Materials and Design 193 (2020) 108776

Contents lists available at ScienceDirect

Materials and Design

journal homepage: www.elsevier.com/locate/matdes

Microstructure evolution and elemental diffusion behavior near the interface of Cr_2AlC and single crystal superalloy DD5 at elevated temperatures

Jimeng Li [a], Jing Jing [a], Jian He [b,c,*], Hao Chen [d], Hongbo Guo [a,c]

[a] School of Materials Science and Engineering, Beihang University (BUAA), No. 37 Xueyuan Road, Beijing 100191, China
[b] Research Institute of Frontier Science, Beihang University (BUAA), No. 37 Xueyuan Road, Beijing 100191, China
[c] Key Laboratory of High-Temperature Structural Materials and Coatings Technology (Ministry of Industry and Information Technology), Beihang University (BUAA), No. 37 Xueyuan Road, Beijing 100191, China
[d] Department of Mechanical, Materials and Manufacturing Engineering, Faculty of Science and Engineering, University of Nottingham Ningbo China, Ningbo 315100, China

HIGHLIGHTS

- Microstructure evolution and interdiffusion behavior of Cr_2AlC/DD5 couple are studied at 1100 °C, 1150 °C, and 1200 °C.
- Diffusion zones composed of different phases are found near the Cr_2AlC/DD5 interface.
- Diffusion model is built based on the results of experimental detection and Thermo-Calc software.
- Al has higher diffusion rate and lower diffusion activation energy due to the weak Cr—Al and Al—Al bonds.

GRAPHICAL ABSTRACT

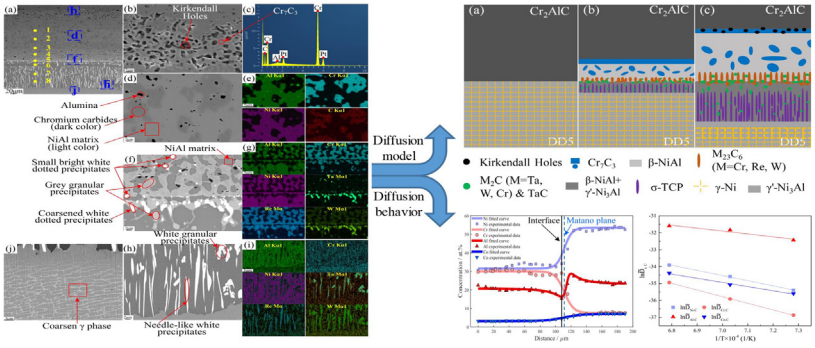

ARTICLE INFO

Article history:
Received 5 March 2020
Received in revised form 16 April 2020
Accepted 1 May 2020
Available online 03 May 2020

Keywords:
Cr_2AlC
Superalloy
Interdiffusion
Microstructure
Diffusion coefficient
Activation energy

ABSTRACT

As one of the promising MAX phase materials for high-temperature applications, Cr_2AlC is considered as a potential substitution bond coat material in thermal barrier coating systems. In this paper, the microstructure evolution and elemental diffusion behavior near the interface of the diffusion couple composed of Cr_2AlC and single crystal superalloy DD5 were investigated at 1100 °C, 1150 °C, and 1200 °C. Elemental interdiffusion between Cr_2AlC and DD5 occurs significantly, resulting in the formation of a thick layer of Kirkendall holes after 20 h heat treatment at 1100 °C and higher temperatures. The outward diffusion of Ni into Cr_2AlC and the inward diffusion of Al into DD5 alloy causes the formation of β-NiAl matrix embedded with dispersed Cr_7C_3 phase. Simultaneously, the precipitation of σ-TCP phase and degradation of the γ/γ′ matrix occurs in the alloy. Additionally, TaC, M_2C (where M = Ta, W, Cr), and $M_{23}C_6$ (M = Cr, Re, W) compounds are formed near the interface along with the dissolution of σ-TCP phases. It is further found that Al in Cr_2AlC exhibits the highest average effective diffusion coefficient among the four dominant diffusing elements. It also displays the lowest diffusion activation energy which is due to its relatively weak Cr—Al and Al—Al bonds.

* Corresponding author at: Research Institute of Frontier Science, Beihang University (BUAA), No. 37 Xueyuan Road, Beijing 100191, China.
E-mail address: hejian511690@buaa.edu.cn (J. He).

https://doi.org/10.1016/j.matdes.2020.108776

1. Introduction

Thermal barrier coatings (TBCs) are protective coating systems that aim to extend the lifetime of high temperature components of turbine engines by improving the high-temperature oxidation and corrosion resistance while simultaneously reducing the working temperature of the metallic substrate [1,2]. Normally, a TBCs system is composed of a ceramic top coat (TC), a metallic bond coat (BC) and a thermally grown oxide (TGO) layer between them [3,4]. The TC usually provides thermal insulation for the underlying parts. The BC together with the TGO protects the metallic substrate from being oxidized during service and allows effective adhesion with the TC. 6–8 wt% Y_2O_3 stabilized ZrO_2 (YSZ) has been the preferred TC material due to its high thermal stability and low thermal conductivity at high temperatures [5]. MCrAlY (where M = Ni and/or Co) is the widely applied traditional BC material but facing severe challenges as the inlet gas temperatures of turbine engines keep increasing. The over-thickened TGO in MCrAlY causes the built-up of thermal stresses in the oxide/coating interface, leading to the crack propagation in the oxide layer and detrimental failure of the TBC system especially under the working temperature higher than 1100 °C [6–8]. Although β-NiAl coating as the promising candidate BC material is used at temperatures above 1200 °C due to its high melting point and good resistance to static oxidation, the poor cyclic oxidation resistance and adhesion of the oxide scale limit its further applications [9,10]. Meanwhile, the degradation of the mechanical properties of the Ni-based superalloy also occurs due to the severe interdiffusion between β-NiAl and its superalloy substrate [9,11]. At present, most studies on NiAl bond coat materials focus on improving the adhesion of oxide scale and reducing the growth of the oxide scale rate by adding Pt and other active elements or developing β-NiAl/γ′-Ni_3Al dual-phase coatings [12–14]. Since the cost of Pt modified NiAl coatings remains a major concern, it is important to find an alternative and cost-effective BC material which has excellent high temperature oxidation resistance and good compatibility with superalloy substrates. One of the materials which arose the research interest is the “MAX” phase materials.

It has been more than a half-century since V.H. Nowotny [15] firstly reported a large family of ternary early transition metal carbides and nitrides in the 1960s. These ternary carbides and nitrides have not been greatly investigated until M.W. Barsoum et al. synthesized high-purity Ti_3SiC_2 phase by hot pressing for the first time in the 1990s [16]. Later, this family of ternary layered compounds was named as “$M_{n+1}AX_n$” phases or “MAX” phase (where M is an early transition metal, A is an A-group element, X is either C or N, and n = 1, 2, or 3 [17]) by M.W. Barsoum [18,19]. $M_{n+1}AX_n$ phases are layered, hexagonal structures (space group D^4_{6h}-$P6_3/mmc$) where nearly close-packed M_6X octahedra are interleaved with pure A atomic layers [20,21]. According to the unique structure, M-X covalent or ionic bonds and M-A (and A-A) metallic bonds coexist in the same crystal, which affords a combination of the performances of ceramics and metals for the MAX phase [22]. In general, MAX phases not only exhibit unique characteristics such as low density, high elastic modulus, and corrosion resistance like ceramics, but also exhibit good machinability, high thermal and electric conductivity, and damage tolerance like metals [23]. High-temperature oxidation behavior studies of Ti_3AlC_2 [17], Ti_2AlC [24], and Cr_2AlC [25] indicate that the three MAX phases nearly follow cubic oxidation kinetics at 1000 °C–1200 °C. Therefore, the three materials are proven to be the most promising MAX phases for high-temperature applications and especially can act as substitution materials for traditional bond coats in TBCs [26–29].

Compared with Cr_2AlC, the compatible coefficients of thermal expansion (CTEs) of α-Al_2O_3, Ti_3AlC_2 and Ti_2AlC lead to less thermal stress within the system under thermal-cycling conditions (CETs of Ti_3AlC_2, Ti_2AlC, Cr_2AlC, and α-Al_2O_3 are 9.0×10^{-6} K^{-1}, 9.2×10^{-6} K^{-1}, 13×10^{-6} K^{-1}, and 9.3×10^{-6} K^{-1} respectively [30,31]). Thus, Ti_3AlC_2 and Ti_2AlC have better thermal shock resistance than Cr_2AlC [25,32]. But M. Sokol et al. [33] have studied the compatibilities between Cr_2AlC/Ti_2AlC and superalloy by conducting a thermal cycling test at 1000 °C with Ti_2AlC/Inconel 718/Cr_2AlC diffusion couple. The result shows that delamination cracks are found near the interface of Ti_2AlC/superalloy after 8 cycles while there is no crack at the interface of Cr_2AlC/superalloy even after 20 cycles. M. Sokol attributed it to the CTEs mismatch between Ti_2AlC and the superalloy (CTE is usually $>15 \times 10^{-6}$ K^{-1} at temperatures higher than 1000 °C [34]). Accordingly, the better capability with the superalloy substrates proves Cr_2AlC is a better substitution bond coat material than Ti_2AlC under the proper working temperature. Work concerned on the fabrication of high-purity Cr_2AlC coatings through cold spraying and HVAPS (high-velocity atmospheric plasma spray) has been reported [35,36]. But previous works mainly focused on the properties between the Cr_2AlC layer and the TGO layer, there are limited studies on the compatibilities and interdiffusion between Cr_2AlC and the superalloy substrate under elevated temperatures. J.L. Smialek et al. [37,38] studied the interdiffusion of Cr_2AlC and LSHR (a superalloy developed by NASA) under 800 °C/100 h treatment and analyzed the microstructure evolution near the interface. But no further research has been reported on the microstructure evolution between Cr_2AlC and single crystal superalloy at even higher temperatures.

Therefore, the aim of this research is to study the microstructure evolution caused by the interdiffusion and quantify the elemental diffusion behavior near the interface of Cr_2AlC and single crystal superalloy at 1100 °C, 1150 °C, and 1200 °C. The Cr_2AlC and single crystal superalloy DD5 diffusion couples were prepared and diffusion treatment was conducted at different temperatures in an argon atmosphere. Microstructure evolution across the Cr_2AlC and DD5 superalloy interface was analyzed. In addition, the average effective diffusion coefficients and diffusion activation energies of Ni, Al, Cr, and Co were obtained in order to quantitatively evaluate their diffusion behavior in this system.

2. Experimental procedures

2.1. The synthesis of bulk Cr_2AlC

The synthesis of bulk Cr_2AlC consists of the following two steps: the pressureless synthesis of pure Cr_2AlC powder, and the densification process by spark plasma sintering (SPS). Chromium (Cr, 99.5% purity), graphite (C, 99.95% purity), and aluminum (Al, 99.5% purity) powders (all from Aladdin, China) were used as starting materials. Cr powder was preferentially milled for 4 h at 400 r.p.m. to reduce its size (D50 ≈ 16 μm) due to its relatively higher hardness. After that, Al powder, C powder, and milled Cr powder with a mole ratio of 1.1:1:2 were milled for 8 h at 350 r.p.m. to reduce the size of the powders (D50 ≈ 19 μm) and mix the powders homogeneously. All milling processes were operated by a planetary milling machine under an argon atmosphere to avoid oxygen contamination. The mixed powder was heated up to 1100 °C under 10^{-3} Pa with an average heating and cooling rate of 7 °C/min and isothermally held for 8 h. The synthesized pure Cr_2AlC was subsequently ground in an agate mortar. Finally, the densification process was carried out by spark plasma sintering (SPS) at 1050 °C under 20 Pa, with uniaxial pressure of 40 MPa and an isothermal holding time of 10 min. Fig. 1a presents the cross-sectional SEM morphology of the bulk Cr_2AlC after the densification process. It can be seen that some voids and impurities, such as alumina, are contained in the densified Cr_2AlC during the milling and densification process. X-ray diffraction was measured by the D/MAX-2500 diffractometer (Rigaku Co.). Rietveld refinement of X-ray diffraction result (as shown in Fig. 1b) identifies that the purity of bulk Cr_2AlC is higher than 97 wt%.

2.2. Cr2AlC/DD5 diffusion couples

Single crystal superalloy DD5 was a Ni-base superalloy with the nominal composition shown in Table 1. The bulk Cr_2AlC were cut into

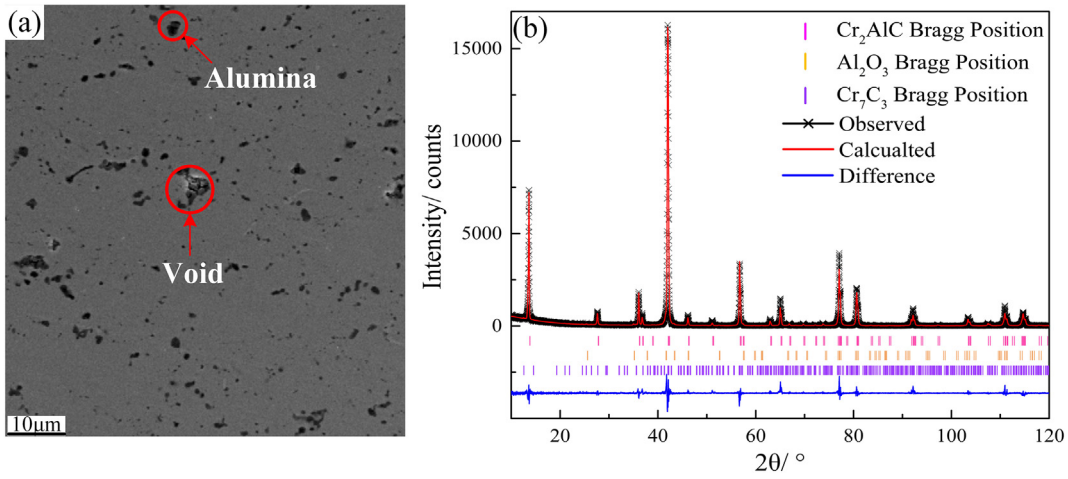

Fig. 1. (a) Cross-sectional secondary electron (SE) SEM morphology of bulk Cr_2AlC after SPS process. (b) X-ray diffraction pattern of bulk Cr_2AlC with Rietveld refinement.

Table 1
The nominal composition of the DD5 single-crystal superalloy (wt%).

Ni	Al	Co	Cr	Mo	W	Re	Ta	Hf	C
Bal.	6.2	8	7	2	5	3	7	0.15	0.05

Φ12 mm × 5 mm circular slices and DD5 superalloy were cut into Φ10 mm × 5 mm circular slices along [001] direction. Both were mechanically ground and polished to 0.5 μm surface finish. The polished surfaces of Cr_2AlC and DD5 alloy specimens were placed and clamped with each other in a special jig to form the diffusion couples. All diffusion couples together with the jigs were annealed for 1 h in a vacuum furnace (10^{-3} Pa) at 1100 °C, 1150 °C, and 1200 °C, respectively, to ensure sufficient adhesion. Subsequently, adhesive diffusion couples were sealed in quartz tubes under argon atmosphere without jigs for the sustained diffusion treatment in a tube furnace at 1100 °C, 1150 °C, and 1200 °C for 20 h and 50 h, respectively.

2.3. Sample characterization

After the diffusion annealing process, diffusion couples were cut by a diamond wire cutting machine to obtain the cross-sections. Polished cross-sections were prepared by the standard metallographic process. The cross-sectional microstructure and elemental distributions were investigated by the scanning electron microscope (SEM, GeminiSEM 300, Zeiss) equipped with an energy dispersive spectrometer (EDS, IE250X-Max50, Oxford Instruments). The elemental concentrations were analyzed by the electron probe microanalyzer (EPMA, JXA-8100, JEOL). The image analysis method was applied to measure the thicknesses of the diffusion regions by ImageJ software.

2.4. Average effective diffusion coefficient and diffusion activation energy

According to the work by M.A. Dayananda [39], in a complex diffusion system with multi-components, an average effective interdiffusion coefficient for component i, $\tilde{D}_{i,C}$, can be applied to describe the diffusion behavior of the component. $\tilde{D}_{i,C}$ is calculated by the following formula:

$$\tilde{D}_{i,C} = \frac{\int_{C_i^+}^{C_i^-} (x-x_0)^2 dC_i}{mt\left(C_i^- - C_i^+\right)} \quad (1)$$

where C_i is the concentration of component i and $m = 2$ if the movement of the boundaries of the diffusion system follows parabolic law, x is the diffusion distance, t is diffusion time, C_i^- and C_i^+ are the concentrations at $x = -\infty$ and $x = +\infty$, x_0 is the location of Matano plane.

After getting the average effective interdiffusion coefficient, the diffusion activation energy of component i can be determined by the equation [40]:

$$\tilde{D}_{i,C} = D_0 \exp\left(-\frac{Q_{d,i}}{RT}\right) \quad (2)$$

where T is temperature, D_0 is diffusion constant, R is gas constant and $Q_{d,i}$ is the activation energy for diffusion of component i.

Thus, in a multicomponent diffusion system, the diffusion rate of an element can be quantitatively evaluated and compared, and the diffusion behavior of the component can also be roughly estimated.

3. Results and discussion

3.1. Diffusion process

Fig. 2 shows the cross-sectional backscattered electron (BSE) morphologies of the initial 1 h annealing treatment at 1100 °C, 1150 °C, and 1200 °C, respectively. It can be seen that the two slices are in good contact and completely bonded with each other. Severe interdiffusion occurred between Cr_2AlC and DD5 alloy so that obvious diffusion regions with different precipitates appear on both sides of the interface. Except that the thickness of the diffusion region (black arrows in Fig. 2) increases as increasing the diffusion temperature, the microstructures of the diffusion regions at the three temperatures are almost the same. Under each diffusion treatment, a region consists of grey granular precipitates (yellow arrows in Fig. 2) can be found near the interface in Cr_2AlC. White dotted precipitates are densely distributed at the interface. White needle-like precipitates together with white granular precipitates appear in the diffusion region of DD5 alloy. Meanwhile, a gap only consisting of grey granular and white dotted precipitates appears between the needle-like precipitates and the interface (the black boxes in Fig. 2). Similarly, the grey granular precipitates region and the gap also become thicker as increasing the temperature.

1200 °C/1 h diffusion couple which suffered the most severe diffusion was chosen as an example to better identify the main diffusion element. Fig. 3 presents the cross-sectional morphology (Fig. 3a) and corresponding EDS elemental mappings (Fig. 3b–e) of the 1200 °C/1 h diffusion couple. According to the elemental mappings, interdiffusion between Cr_2AlC and DD5 alloy is mainly caused by the diffusion of Al and Cr from Cr_2AlC to DD5 alloy and the outward diffusion of Ni and Co in DD5 alloy to Cr_2AlC. The diffusion of Al leads to the formation of the Al depletion region on the Cr_2AlC side (the yellow box in Fig. 3c).

The morphologies of cross-sections near the interface of Cr_2AlC/DD5 diffusion couples annealed at 1100 °C, 1150 °C, and 1200 °C for different

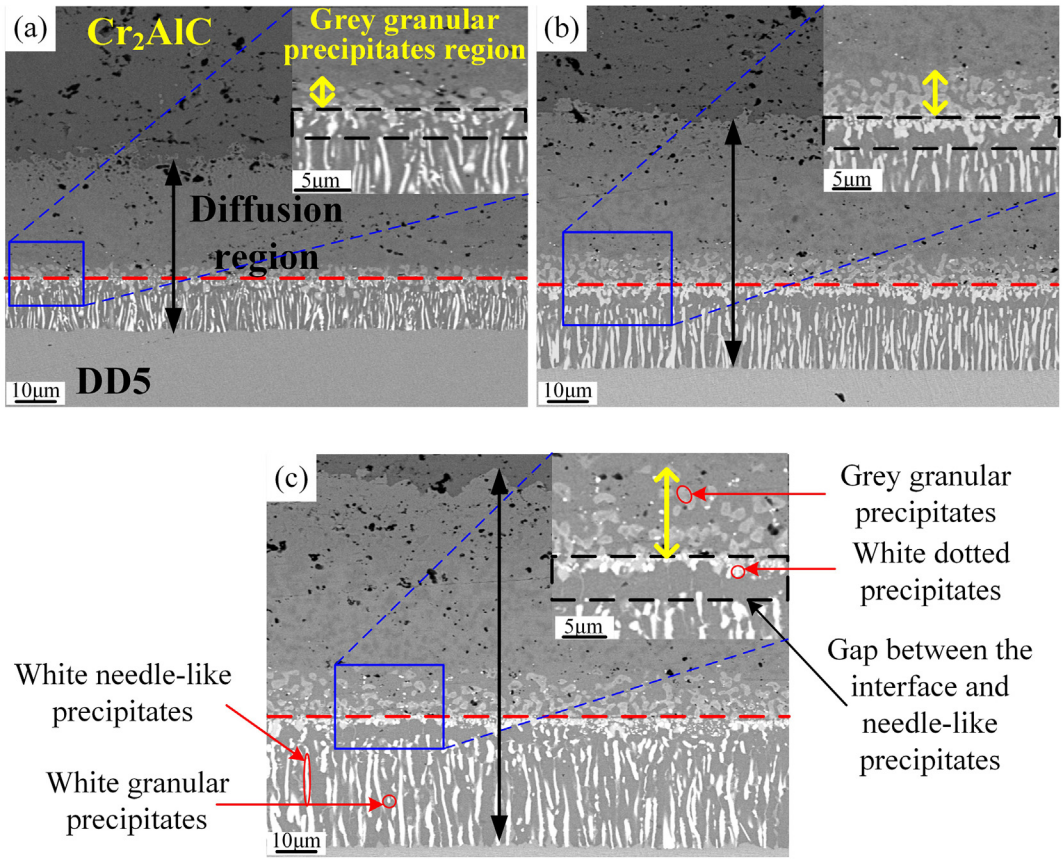

Fig. 2. Cross-sectional backscattered electron (BSC) SEM morphologies near the interface (red dash line) of the diffusion couple after 1 h initial annealing treatment. (a) 1100 °C. (b) 1150 °C. (c) 1200 °C. In each figure, the black arrow shows the diffusion region; the higher magnification morphology is the blue dashed square region; the yellow arrow shows the grey precipitates region; the black dotted box shows the gap between the interface and the needle-like precipitates.

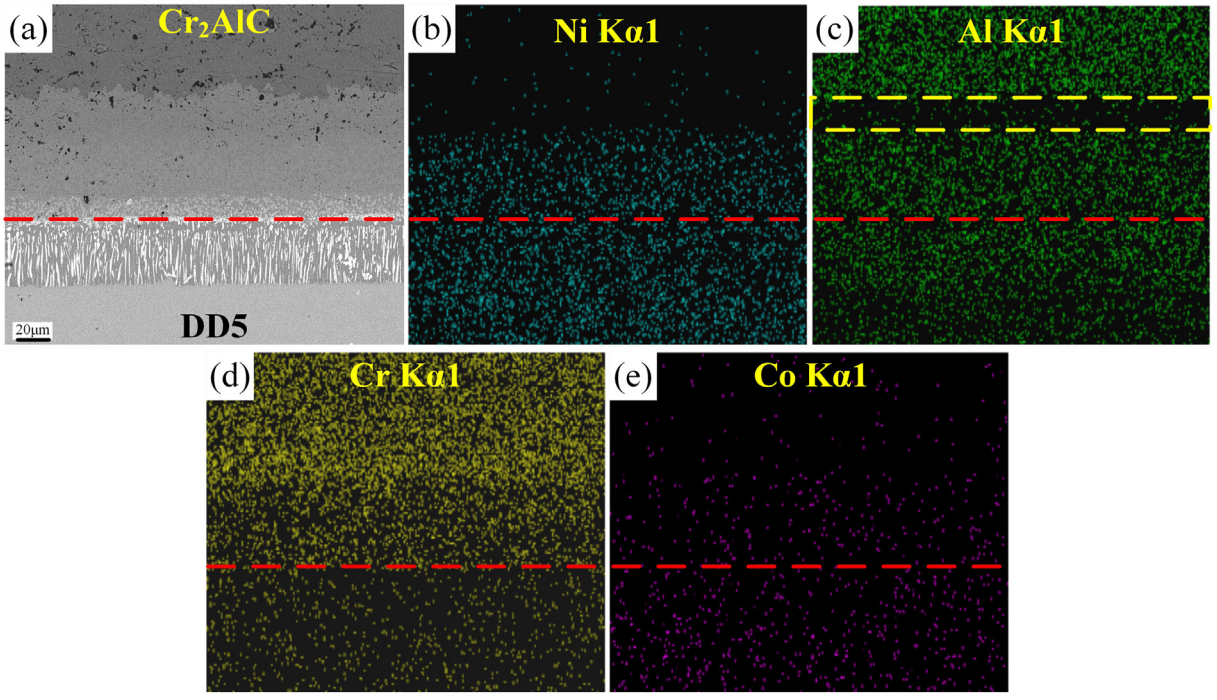

Fig. 3. (a) Cross-sectional BSE SEM morphology of 1200 °C/1 h diffusion couple. (b)–(e) Corresponding elemental mappings by EDS. The red dash line is the interface and the yellow dotted box in (c) is Al depletion zone.

hours are shown in Fig. 4. Fig. 4a to c and d to f exhibit the microstructures close to the interface of couples after annealing for 20 h and 50 h, respectively. It can be seen that the diffusion region gradually extends under longer diffusion time and higher diffusion temperatures. Two characteristic regions, i.e., the grey granular precipitates region and the gap between the needle-like precipitates and the interface, still exist. But unlike the microstructures of 1-h treatment, a region consisting of holes (the yellow dotted boxes in Fig. 4) appears in the diffusion region of Cr_2AlC away from the interface after the long-time treatment. The region of holes also becomes thicker as the increased time and temperature. The thicknesses of the diffusion regions in Cr_2AlC and DD5 alloy and the two characteristic regions under each diffusion treatment were measured by the image analysis method. The results are plotted vs. the square root of the diffusion time in Fig. 5. It presents that the growth of the diffusion regions and the two characteristic regions under the three temperatures are nearly proportional to the square root of the diffusion time. Accordingly, the movements of the boundaries of the entire diffusion region and the characteristic regions within it follow the parabolic law.

3.2. Phase identification

As shown in Fig. 6, the Cr_2AlC/DD5 diffusion couple which was annealed at 1200 °C for 20 h (Fig. 6a) is used as an example to clearly examine the microstructure of the diffusion region near the interface. A region consisting of holes (Fig. 6b) appears in the diffusion region of Cr_2AlC away from the interface. The EDS spectrum of the part around the holes is shown in Fig. 6c. As can be seen, Al content is extremely low, and the main constituent elements are Cr and C. According to the findings by J.L. Smialek [38], the chromium carbide should be Cr_7C_3 phase. As a consequence, the holes surrounded by Cr_7C_3 are Kirkendall holes formed by the outward diffusion of Al atoms. Fig. 6d and e show the microstructure and the elemental distribution of the region below Kirkendall holes. The darker-colored chromium carbides are distributed in the light-colored nickel aluminum matrix (the black dots are alumina impurities). It is believed that NiAl is formed by the outward diffusion of Ni atoms from DD5 alloy and the inward diffusion flux of Al atoms from Cr_2AlC. When Al atoms escape from Cr_2AlC, chromium carbides are formed by the remaining Cr atoms and C atoms and are distributed in the NiAl matrix.

The microstructure and elemental distribution close to the interface are shown in Fig. 6f and g. On the side of Cr_2AlC near the interface, closely-arrayed grey granular precipitates are distributed in the NiAl matrix, and small bright white dotted precipitates appear around them. Additionally, grey granular precipitates and coarsened white dotted precipitates are densely distributed on the side of DD5 alloy near the interface. According to the EDS elemental distribution, the grey granular precipitates are mainly composed of Cr, Re and a small amount of W, while the white dotted precipitates are mainly consisting of Cr, Ta, and W. The aluminum-rich black dots in Fig. 6f are alumina impurities

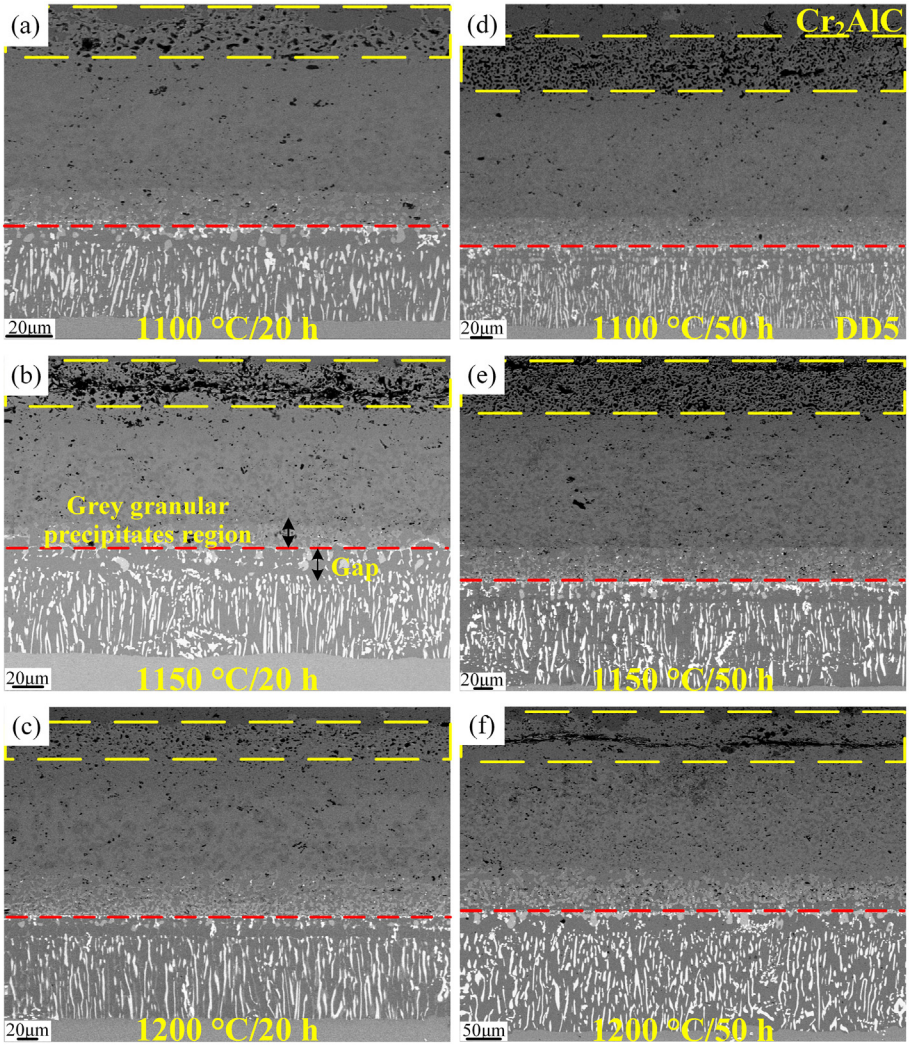

Fig. 4. Cross-sectional BSE SEM morphologies near the interface (red dash line) of the diffusion couple after different diffusion treatments. (a) 1100 °C/20 h. (b) 1150 °C/20 h. (c) 1200 °C/20 h. (d) 1100 °C/50 h. (e) 1150 °C/50 h. (f) 1200 °C/50 h. The yellow dotted box in each figure shows the Kirkendall hole region.

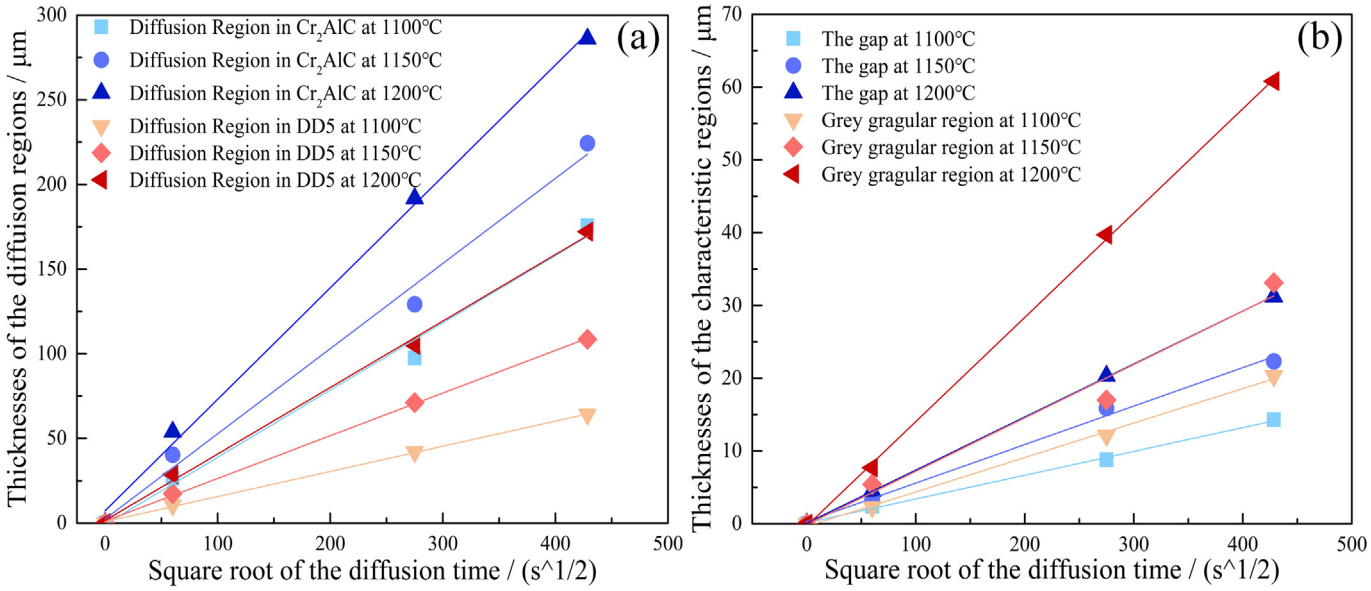

Fig. 5. (a) The thicknesses of the diffusion regions in Cr_2AlC and DD5 alloy under different temperatures vs. the square root of the diffusion time. (b) The thicknesses of the characteristic diffusion regions under different temperatures vs. the square root of the diffusion time.

formed during the synthesis of Cr_2AlC. It can be seen from Fig. 6h and i that the refractory elements Ta, W, and Re are enriched in the needle-like white precipitates away from the interface in the diffusion region of DD5 alloy and the white granular precipitates around them are rich in Ta and W by comparison. Accordingly, the needle-like white precipitates are topologically closed-packed (TCP) phases due to the precipitation of the refractory elements during the phase transformation from the coherent γ/γ′ to γ′ or even to β caused by the diffusion of Al and Ni in the opposite directions [41]. As shown in Fig. 6j, Slight rafting as well as the coarsening of γ phase occurs below the diffusion region of the DD5 alloy indicating the degradation of the coherent γ/γ′ microstructure.

Thermo-Calc Software is used to identify the phase compositions of the whole diffusion region in this study. The elemental concentrations of the representative 8 positions in the diffusion region (as shown in Fig. 6a) were firstly determined by EPMA, and the phase compositions of each point were calculated by Thermo-Calc software. The calculation results are shown in Table 2. It can be seen that the light-colored matrix phase below the Kirkendall hole region is β-NiAl, and the dark chromium carbides distributed within the matrix are Cr_7C_3, which is consistent with the results described above. In the vicinity of the diffusion couple interface, the grey granular precipitates are $M_{23}C_6$ type carbides (where M = Re, W, and Cr), while the white dotted precipitates including the densely distributed coarsened ones at the interface are M_2C type carbides (where M = Ta, W, Cr) and TaC. The matrix of the diffusion region of DD5 alloy is basically comprised of β-NiAl and γ′-Ni_3Al, and the white needle-like precipitates distributed in the matrix are σ-TCP phases. Meanwhile, the granular white precipitates around σ-TCP phases are also M_2C type carbides (where M = Ta, W, Cr) and TaC.

As mentioned above, the thickness of the region containing $M_{23}C_6$ (where M = Re, W, and Cr) type carbides and the gap between the interface and σ-TCP phases are gradually extended. It most likely corresponds to the microstructure evolution of the precipitates near the interface. Similar to the findings reported by E.C. Santos et al. [42], the dissolution of the σ-TCP phases close to the interface occurs during the diffusion process which accounts for the increases of the gap. Yet the M_2C type (where M = Ta, W, Cr) and TaC carbides mostly remain in the gap without dissolution. Simultaneously, the dissolved refractory elements, especially Re, diffuse towards Cr_2AlC side under the attraction of a high concentration of Cr atoms and thus form stable $M_{23}C_6$ type carbides (where M = Re, W, and Cr) close to the interface. Consequently, as the continuous dissolution of the σ-TCP phase, the thickness of the region containing $M_{23}C_6$ type carbides (where M = Re, W, and Cr) and the gap between the interface and σ-TCP phases gradually increase with longer diffusion time and higher diffusion temperature.

A diffusion model (Fig. 7) for Cr_2AlC/DD5 couples is established in terms of the results calculated by Thermo-Calc software. As demonstrated in Fig. 7a and b, initial interdiffusion between Cr_2AlC and DD5 alloy occurs during the 1 h annealing treatment, among which Al atoms in Cr_2AlC diffuse towards DD5 alloy and Ni atoms in DD5 diffuse backwards. As a result, the main phase of the diffusion region of Cr_2AlC transfers into β-NiAl in which Cr_7C_3 carbides are dispersed. Simultaneously, the DD5 diffusion region changes from the original γ-Ni/γ′-Ni_3Al phase to β-NiAl/γ′-Ni_3Al phase. In addition, the refractory elements near the interface diffuse into Cr_2AlC leading to the formation of the grey granular $M_{23}C_6$ (M = Re, W, Cr) carbides and white dotted M_2C (M = Ta, W, Cr) carbides and TaC on both sides of the interface. Due to the degradation of the original γ-Ni/γ′-Ni_3Al phase accompanied by the decrease in the solubility of the refractory elements, the refractory elements precipitate to form needle-like σ-TCP phases and white granular M_2C (M = Ta, W, Cr) carbides and TaC in the diffusion region of DD5 alloy.

As the diffusion time goes on or the diffusion temperature rises, the thicknesses of the diffusion regions in Cr_2AlC and DD5 alloy both increase, as shown in Fig. 7c. Kirkendall holes develop in the top area of the diffusion region of Cr_2AlC due to the continued loss of Al atoms. Furthermore, with the dissolving of σ-TCP phases, the thickness of the $M_{23}C_6$ (M = Re, W, Cr) enriched region and the gap between the interface and σ-TCP phases increase gradually.

3.3. Diffusion activation energy

Various elements are involved in Cr_2AlC/DD5 diffusion system, however, in order to simplify the research, only the dominant diffusing elements, i.e., Ni, Cr, Al, and Co, are considered in this study. The compositions of Ni, Al, Cr, and Co on both sides of the interface after 1100 °C/20 h, 1150 °C/20 h, and 1200 °C/20 h diffusion treatments were determined by EPMA. As an example, Fig. 8 shows the distribution of Ni, Cr, Al and Co along the cross-section of the Cr_2AlC/DD5 couple after 1200 °C/20 h diffusion treatment. Noteworthily, it seems an uphill diffusion of Al occurred in Cr_2AlC/DD5 couple. To find out the reason, a detailed investigation has been carried out. Fig. 9 shows the phase

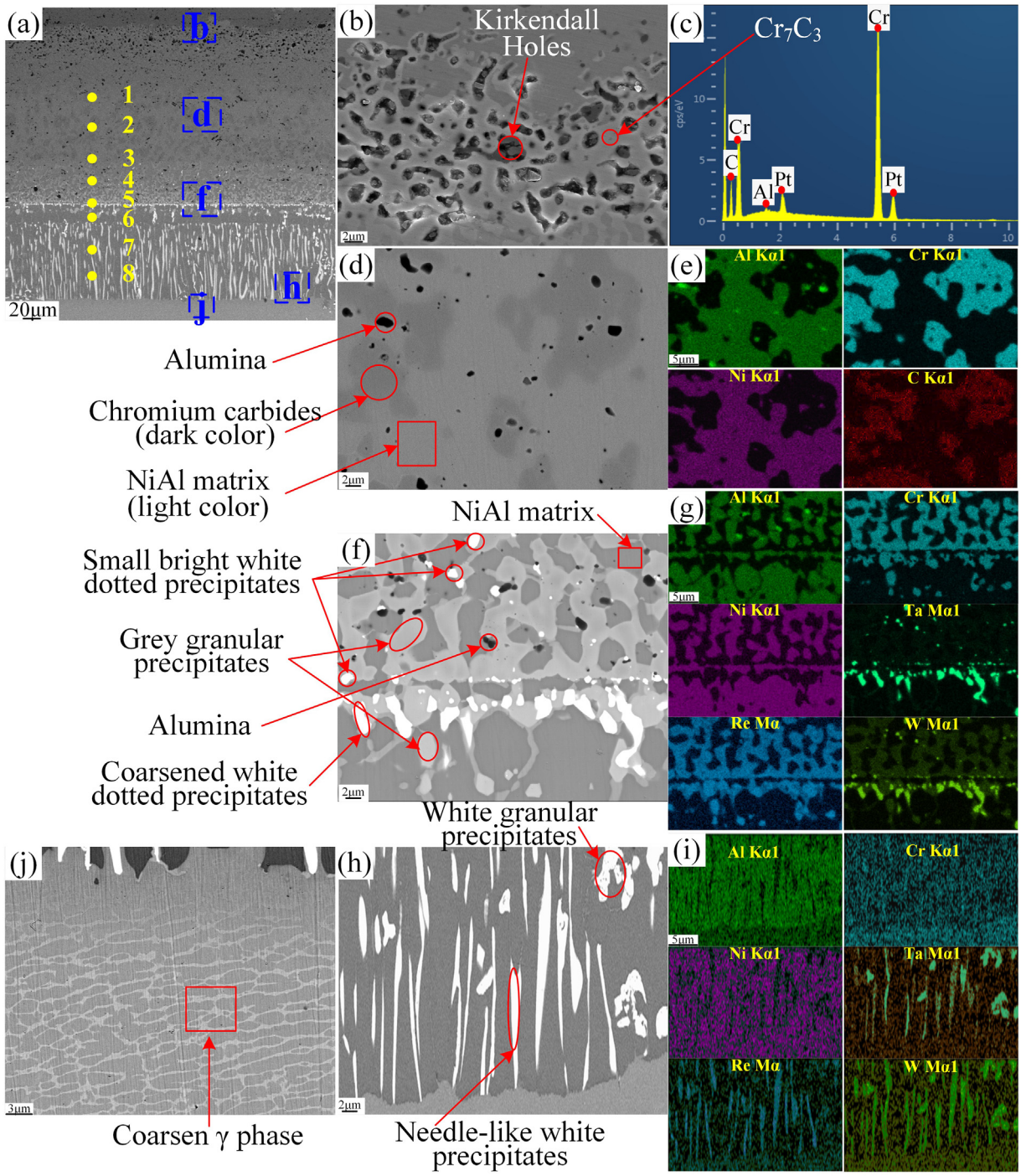

Fig. 6. (a) Cross-sectional BSE SEM morphologies of 1200 °C/20 h diffusion couple. (b), (d), (f), (h), and (j) are higher magnification morphologies of the blue dashed box in (a). (c), (e), (g), and (i) are corresponding elemental analysis by EDS. (Fig. 4b is the SE SEM morphology of Kirkendall holes, others are BSE SEM morphologies). Point 1 to Point 8 are eight representative positions used to calculate phase compositions by Thermo-Calc software.

contents (in mol.%) of β-NiAl and γ′-Ni_3Al at the 8 representative positions together with the corresponding total Al contents (in at.%) in the two phases. It should be noted that the total Al content in β (or γ′) phase equals to the product of the phase content of β (or γ′) and the corresponding Al content in the phase, while the total Al content at the position is the sum of the total Al content in β and γ′ phases at the specified position. It is found that the trend of the total Al content at the 8 positions quite fits the EPMA results, indicating that Al is mainly contained in β and γ′ phases. Due to the increase of the carbides ($M_{23}C_6$ (where M = Re, W, and Cr), M_2C (where M = Ta, W, Cr), and TaC) in the Cr_2AlC near the interface, the phase content of β-NiAl decreases towards the interface. Since Al mainly exists in β-NiAl and no γ′-Ni_3Al exists in the Cr_2AlC diffusion region, its total Al content tends to decrease towards the interface, suggesting continuous diffusion of Al from Cr_2AlC to the interface. However, β-NiAl and γ′-Ni_3Al coexist in the diffusion region of DD5 alloy. In the gap between the interface and σ-TCP phases, it contains much more β-NiAl with gradually reduced carbides ($M_{23}C_6$ (where M = Re, W, and Cr), M_2C (where M = Ta, W, Cr), and TaC), while in the areas away from the gap, it contains more γ′-Ni_3Al with a large quantity of σ-TCP phases. Therefore, in the DD5

Table 2
Phase compositions (in mol.%) of each position in 1200 °C/20 h diffusion couple calculated by Thermo-Calc software.

Position	β-NiAl	Cr_7C_3	$M_{23}C_6$ (M = Cr, Re, W)	γ′-Ni_3Al	M_2C (M = Ta, W, Cr) & TaC	σ-TCP
1	61.9	38.1				
2	62.5	37.5				
3	60.4	39.6				
4	55.1	19.6	17.7		7.5	
5	38.0	10.2	32.4	15.9	3.5	
6	62.9			28.7	8.5	
7	58.3			33.2	4.2	4.4
8	44.1			47.5	4.1	4.3

diffusion region, the total Al content firstly increases at the gap and then decreases away from the gap. To sum up, the lowest Al content appears at the Cr_2AlC/DD5 interface, and the highest Al content is achieved at the gap between the interface and σ-TCP phases. It seems that β-NiAl phase formed at the gap acts as a transitional Al reservoir because the inward Al diffusion is slowed down by the large quantity of σ-TCP phases. Undoubtedly from the perspective of the whole diffusion process, Al diffuses from Cr_2AlC with a higher content to DD5 alloy with lower content.

It can be seen from Fig. 8, without considering the Kirkendall holes region and the external region, the diffusion concentration-distance curves of Ni, Co, and Cr close to the interface follow the concentration gradient and are similar to the typical diffusion curves for the diffusion region. Thus in this study, the region between the black dash-dotted lines in Fig. 8 (marked as "main diffusion region") is treated as the target area to quantitatively evaluate the diffusion rate of Ni, Al, Cr, and Co on both sides of the Cr_2AlC/DD5 interface. And the Average effective diffusion coefficients for the four dominant diffusing elements are accordingly obtained. The concentration-distance curves close to the interface are fitted according to the Boltzmann function and finally presented in Fig. 10. Considering that the Al distribution shown on the curve exhibits an opposite diffusion trend compared to the original concentration gradient in Cr_2AlC/DD5 couple, the concentration-distance curve of Al is fitted by the least square method [43].

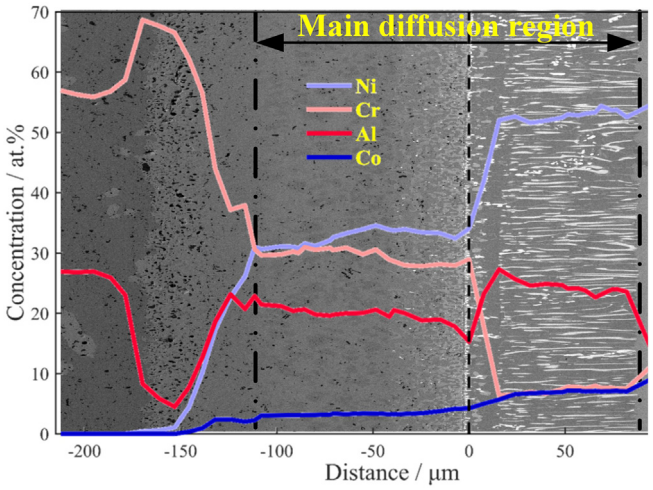

Fig. 8. The concentration-distance profiles of Ni, Cr, Al, and Co across the interface (dash line) of 1200 °C/20 h diffusion couple. The region between the dotted dash lines is the main diffusion region.

According to Formula (1), the average effective diffusion coefficients, $\tilde{D}_{i,C}$, can be applied to evaluate the diffusion rate of the four dominant elements. C_i^+ and C_i^- were obtained according to the fitted curves. Since the movements of the boundaries of the diffusion regions follow parabolic law, m equals 2 in this study. $\tilde{D}_{i,C}$ obtained at 1100 °C, 1150 °C, and 1200 °C are listed in Table 3. It is worth noting that the calculated values of $\tilde{D}_{Al,C}$ are negative, which corresponds to the uphill diffusion of Al [44], and the absolute values of $\tilde{D}_{Al,C}$ are shown in the table. It can be found that $\tilde{D}_{Al,C}$ is the largest, while $\tilde{D}_{Cr,C}$ is the smallest. $\tilde{D}_{Al,C}$ is about 1– 2 orders of magnitude higher than that of the other three elements indicating a higher diffusion rate of Al. Since the inward diffusion rate of Al from Cr_2AlC is much faster than the outward diffusion rate of Ni from DD5 alloy, a net diffusion flux from Cr_2AlC to DD5 is generated, leading to the net loss of atoms and the formation of Kirkendall holes on the side of Cr_2AlC.

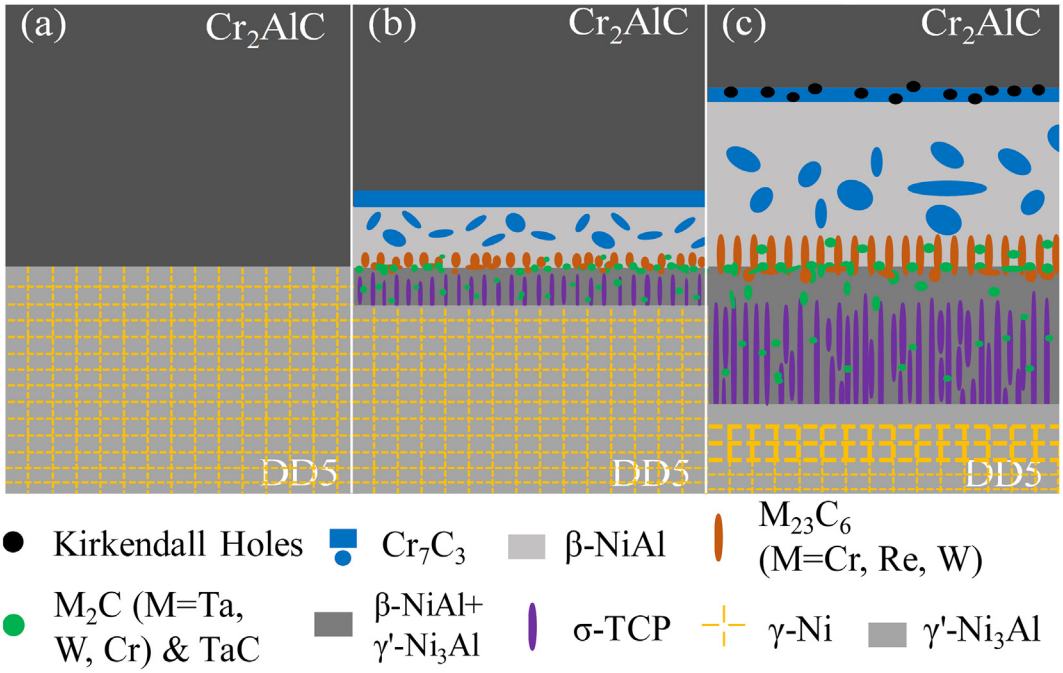

Fig. 7. Schematic of microstructure evolution of Cr_2AlC/DD5 diffusion system at high temperatures: (a) At the beginning without any interdiffusion. (b) Initial interdiffusion occurs. (c) After diffusion treatment for a longer time, Kirkendall holes appear in the Al depletion region.

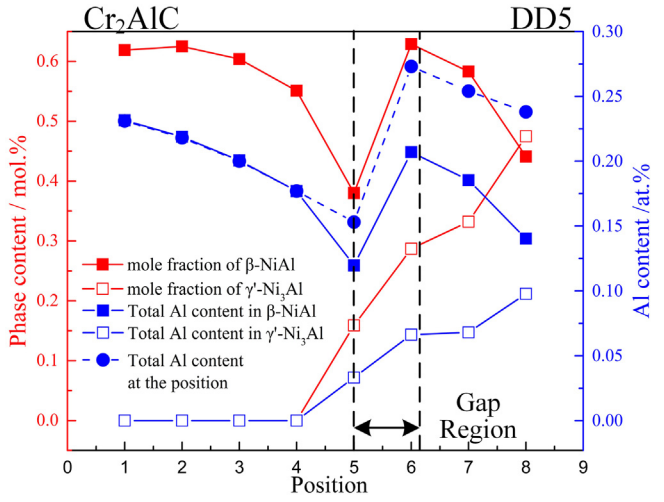

Fig. 9. β-NiAl and γ′-Ni_3Al mole fraction and Al content (at.%) of the 8 representative different positions in 1200 °C/20 h diffusion couple.

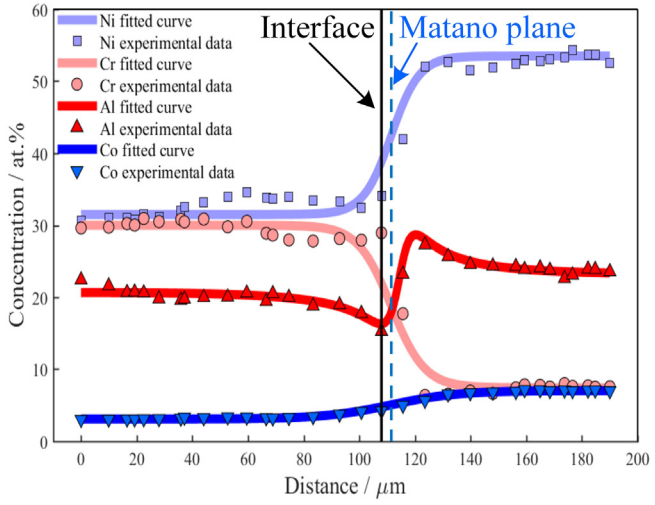

Fig. 10. The EPMA concentration data of 1200 °C/20 h diffusion couple and the fitted concentration-distance curves of element Ni, Cr, Al, and Co.

In order to compare the difficulty of the diffusion, the activation energy of diffusion in this system is also calculated with the obtained $\tilde{D}_{i,C}$ by the transformed Formula (2)

$$\ln\tilde{D}_{i,C} = \ln D_0 - \frac{Q_{d,i}}{RT} \quad (3)$$

where the symbols are consistent with those in Formula (2).

The relationships between $\ln\tilde{D}_{i,C}$ and $1/T$ of the four elements are plotted in Fig. 11. The linear fitted curves are also given. According to Formula (3), the slope of each fitted curve is $Q_{d,i}/R$. Thus, the activation

Table 3
The average effective diffusion coefficient for Ni, Cr, Al, and Co.

Temperature/°C	Average effective diffusion coefficient ($\times10^{-15}$ m^2/s)			
	Ni	Cr	Al	Co
1100	0.4	0.1	8.2[a]	0.3
1150	1.0	0.3	14.9[a]	0.6
1200	1.9	0.7	19.0[a]	1.2

[a] The calculated values for Al are negative, which corresponds to the uphill diffusion, and the absolute values are shown here.

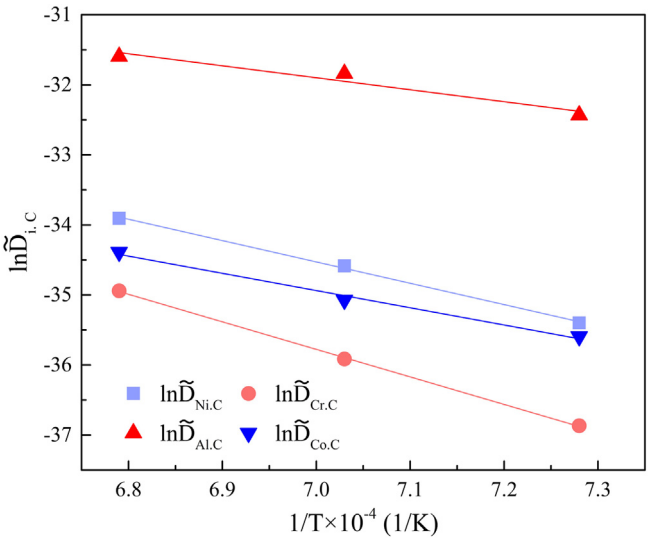

Fig. 11. $\ln(\tilde{D}_{i,C})$ vs. $1/T$ of the four elements at three diffusion temperatures.

Table 4
The comparison of the activation energy of Cr and Al in MCrAlY, NiPtAl, and this work.

Activation energy/kJ/mol	Cr	Al
In MCrAlY[45]	257	268
In NiPtAl [46]		223 ± 19
This work	327 ± 6	142 ± 32

energies of Ni, Cr, Al, and Co are 253 ± 10 kJ/mol, 327 ± 6 kJ/mol, 142 ± 32 kJ/mol, and 203 ± 18 kJ/mol, respectively.

The diffusion activation energies of Al and Cr in Cr_2AlC and the other two traditional bond coat materials, namely MCrAlY [45] and NiPtAl [46] are given in Table 4. As can be seen, Al has the lowest diffusion activation energy in Cr_2AlC which is mainly due to the unique layered structure of Cr_2AlC [20]. In the layered structure, nearly close-packed Cr_6C is interleaved by Al atomic layer, and Al atoms are only restrained by Cr—Al and Al—Al bonds. Due to the weak bond strength, Al atoms are easy to slide over other atoms when they are thermally activated [47]. While in MCrAlY and NiPtAl, the bond strength between Al and other atoms (mainly the covalent-like Ni—Al bonds) is much stronger which can constrain the Al migration [48]. Therefore, compared with the other two traditional bond coat materials, Cr_2AlC has the lowest Al diffusion activation energy, which will trigger a severe interdiffusion with DD5 superalloy substrate. Similarly, the special structural characteristics of Cr_2AlC can also explain why the Cr diffusion activation energy in Cr_2AlC is higher. Cr atoms are mainly restrained by Cr—C σ-bonds in Cr_2AlC [47,49], the bond strength of which is much stronger than the Cr-contained bonds in MCrAlY. On the other hand, Cr atoms in Cr_2AlC will form $M_{23}C_6$ (where M = Re, W, and Cr) type carbides near the interface together with Re and W atoms from DD5. Accordingly, Re and W elements could play a role in pinning the Cr atoms and hence suppress the diffusion of Cr to some extent. Thus, Cr diffusion activation energy in Cr_2AlC is higher than that in MCrAlY.

4. Conclusion

The microstructure evolution and elemental interdiffusion behavior near the interface of Cr_2AlC/DD5 single crystal superalloy diffusion couples were investigated. Some conclusions can be drawn as follows:

(1) Severe interdiffusion occurred between Cr_2AlC and DD5 alloy. The interdiffusion region in Cr_2AlC consisted of β-NiAl matrix and randomly distributed Cr_7C_3. TaC, M_2C (M = Ta, W, Cr)

carbides, and $M_{23}C_6$ (M = Cr, Re, W) compounds formed close to the interface. The γ/γ′ matrix transferred into β/γ′ in DD5 alloy due to the loss of Ni and the replenishment of Al. Accordingly, the refractory elements precipitates of σ-TCP phases, $M_{23}C_6$ (M = Cr, Re, W) and TaC carbides presented in the matrix. Simultaneously, the dissolution of σ-TCP phases also occurred during the diffusion process.

(2) Among the four main diffusion elements, namely Ni, Cr, Co, and Al, Al has the largest average effective diffusion coefficient. Kirkendall hole region appeared on the Cr_2AlC side after long-term diffusion due to the excessive difference in diffusion rate between Al and Ni.

(3) Compared with the traditional bond coat materials, the Cr_2AlC/DD5 system has lower Al diffusion activation energy due to its relatively weak Cr—Al and Al—Al bonds, and higher Cr activation energy due to the strong Cr—C bonds and the affinity with Re and W.

CRediT authorship contribution statement

Jimeng Li: Investigation, Formal analysis, Writing - original draft. **Jing Jing:** Investigation, Formal analysis. **Jian He:** Formal analysis, Writing - review & editing, Supervision, Project administration. **Hao Chen:** Formal analysis. **Hongbo Guo:** Funding acquisition, Supervision, Project administration.

Declaration of competing interest

The authors declare that they have no known competing financial interests or personal relationships that could have appeared to influence the work reported in this paper.

Acknowledgments

This research is sponsored by National Natural Science Foundation of China (NFSC) under grant no. 51590894, National Science and Technology Major Project under grant no. 2017-VI-0010-0081, and Beijing Natural Science Foundation under grant no. 2194078.

References

[1] M.S. Sahith, G. Giridhara, R.S. Kumar, Development and analysis of thermal barrier coatings on gas turbine blades–a review, Mater. Today Proc. 5 (1) (2018) 2746–2751.
[2] R. Vaßen, M.O. Jarligo, T. Steinke, D.E. Mack, D. Stöver, Overview on advanced thermal barrier coatings, Surf. Coat. Technol. 205 (4) (2010) 938–942.
[3] P.G. Lashmi, P.V. Ananthapadmanabhan, G. Unnikrishnan, S.T. Aruna, Present status and future prospects of plasma sprayed multilayered thermal barrier coating systems, J. Eur. Ceram. Soc. 40 (8) (2020) 2731–2745.
[4] H. Xu, H. Guo, Thermal Barrier Coatings, Elsevier, 2011.
[5] X. Cao, R. Vaßen, D. Stöver, Ceramic materials for thermal barrier coatings, J. Eur. Ceram. Soc. 24 (1) (2004) 1–10.
[6] W.R. Chen, X. Wu, B.R. Marple, D.R. Nagy, P.C. Patnaik, TGO growth behaviour in TBCs with APS and HVOF bond coats, Surf. Coat. Technol. 202 (12) (2008) 2677–2683.
[7] W. Zhu, Z.B. Zhang, L. Yang, Y.C. Zhou, Y.G. Wei, Spallation of thermal barrier coatings with real thermally grown oxide morphology under thermal stress, Mater. Des. 146 (2018) 180–193.
[8] Y. Sohn, J. Kim, E. Jordan, M. Gell, Thermal cycling of EB-PVD/MCrAlY thermal barrier coatings: I. Microstructural development and spallation mechanisms, Surf. Coat. Technol. 146 (2001) 70–78.
[9] X. Gong, H. Peng, Y. Ma, H. Guo, S. Gong, Microstructure evolution of an EB-PVD NiAl coating and its underlying single crystal superalloy substrate, J. Alloys Compd. 672 (2016) 36–44.
[10] D. Li, H. Guo, D. Wang, T. Zhang, S. Gong, H. Xu, Cyclic oxidation of β-NiAl with various reactive element dopants at 1200°C, Corros. Sci. 66 (2013) 125–135.
[11] C.M.F. Rae, M.S. Hook, R.C. Reed, The effect of TCP morphology on the development of aluminide coated superalloys, Mater. Sci. Eng. A 396 (1–2) (2005) 231–239.
[12] J. Sun, L. Wei, Q. Li, S. Gong, H. Guo, Microstructure stability of γ′ + β Ni–Al coated single-crystal superalloy N5 annealed at 1100 °C, Rare Metals (2017) 1–8.
[13] C. Oskay, M.C. Galetz, H. Murakami, Oxide scale formation and microstructural degradation of conventional, Pt- and Pt/Ir-modified NiAl diffusion coatings during thermocyclic exposure at 1100°C, Corros. Sci. 144 (2018) 313–327.
[14] C. Jiang, S. Li, H. Liu, Z. Bao, J. Zhang, S. Zhu, F. Wang, Effect of Hf addition in (Ni,Pt)Al bond coat on thermal cycling behavior of a thermal barrier coating system at 1100 °C, Corros. Sci. 166 (2020) 108424.
[15] V.H. Nowotny, Strukturchemie einiger verbindungen der übergangsmetalle mit den elementen C, Si, Ge, Sn, Prog. Solid State Chem. 5 (1971) 27–70.
[16] M.W. Barsoum, T. El-Raghy, Synthesis and characterization of a remarkable ceramic, J. Am. Ceram. Soc. 79 (7) (1996) 1953–1956.
[17] M.W. Barsoum, MAX Phases: Properties of Machinable Ternary Carbides and Nitrides, John Wiley & Sons, 2013.
[18] M.W. Barsoum, The MN+1AXN phases: a new class of solids: thermodynamically stable nanolaminates, Prog. Solid State Chem. 28 (1–4) (2000) 201–281.
[19] M.W. Barsoum, T. El-Raghy, The MAX phases: unique new carbide and nitride materials: ternary ceramics turn out to be surprisingly soft and machinable, yet also heat-tolerant, strong and lightweight, Am. Sci. 89 (4) (2001) 334–343.
[20] O. Berger, C. Leyens, S. Heinze, R. Boucher, M. Ruhnow, Characterization of Cr–Al–C and Cr–Al–C–Y films synthesized by High Power Impulse Magnetron Sputtering at a low deposition temperature, Thin Solid Films 580 (2015) 6–11.
[21] J. Etzkorn, M. Ade, H. Hillebrecht, Ta3AlC2 and Ta4AlC3— single-crystal investigations of two new ternary carbides of tantalum synthesized by the molten metal technique, Inorg. Chem. 46 (4) (2007) 1410–1418.
[22] M. Radovic, M.W. Barsoum, MAX phases: bridging the gap between metals and ceramics, Am. Ceram. Soc. Bull. 92 (3) (2013) 20–27.
[23] M.W. Barsoum, Physical properties of the MAX phases, Encycl. Mater. Sci. Technol. 1 (11) (2006).
[24] W. Yu, M. Vallet, B. Levraut, V. Gauthier-Brunet, S. Dubois, Oxidation mechanisms in bulk Ti2AlC: influence of the grain size, J. Eur. Ceram. Soc. 40 (5) (2020).
[25] J. Gonzalez-Julian, T. Go, D. Mack, R. Vaßen, Thermal cycling testing of TBCs on Cr2AlC MAX phase substrates, Surf. Coat. Technol. 340 (2018) 17–24.
[26] Z. Lin, M. Li, J. Wang, Y. Zhou, High-temperature oxidation and hot corrosion of Cr2AlC, Acta Mater. 55 (18) (2007) 6182–6191.
[27] B. Cui, D.D. Jayaseelan, W.E. Lee, Microstructural evolution during high-temperature oxidation of Ti2AlC ceramics, Acta Mater. 59 (10) (2011) 4116–4125.
[28] J.L. Smialek, Environmental resistance of a Ti2AlC-type MAX phase in a high pressure burner rig, J. Eur. Ceram. Soc. 37 (1) (2017) 23–34.
[29] J. Gonzalez-Julian, T. Go, D.E. Mack, R. Vaßen, Environmental resistance of Cr2AlC MAX phase under thermal gradient loading using a burner rig, J. Am. Ceram. Soc. 101 (5) (2018) 1841–1846.
[30] W. Tian, P. Wang, G. Zhang, Y. Kan, Y. Li, D. Yan, Synthesis and thermal and electrical properties of bulk Cr2AlC, Scr. Mater. 54 (5) (2006) 841–846.
[31] N.J. Lane, S.C. Vogel, E.a.N. Caspi, M.W. Barsoum, High-temperature neutron diffraction and first-principles study of temperature-dependent crystal structures and atomic vibrations in Ti3AlC2, Ti2AlC, and Ti5Al2C3, J. Appl. Phys. 113 (18) (2013) 183519.
[32] J.L. Smialek, B.J. Harder, A. Garg, Oxidative durability of TBCs on Ti2AlC MAX phase substrates, Surf. Coat. Technol. 285 (2016) 77–86.
[33] M. Sokol, J. Yang, H. Keshavan, M.W. Barsoum, Bonding and oxidation protection of Ti2AlC and Cr2AlC for a Ni-based superalloy, J. Eur. Ceram. Soc. 39 (4) (2019) 878–882.
[34] P. Quested, R. Brooks, L. Chapman, R. Morrell, Y. Youssef, K. Mills, Measurement and estimation of thermophysical properties of nickel based superalloys, Mater. Sci. Technol. 25 (2) (2009) 154–162.
[35] T. Go, Y. Sohn, G. Mauer, R. Vaßen, J. Gonzalez-Julian, Cold spray deposition of Cr2AlC MAX phase for coatings and bond-coat layers, J. Eur. Ceram. Soc. 39 (4) (2019) 860–867.
[36] J. Gonzalez-Julian, G. Mauer, D. Sebold, D.E. Mack, R. Vaßen, Cr2AlC MAX phase as bond coat for thermal barrier coatings: processing, testing under thermal gradient loading, and future challenges, J. Am. Ceram. Soc. 103 (4) (2020) 2362–2375.
[37] J.L. Smialek, A. Garg, Microstructure and Oxidation of a MAX Phase/Superalloy Hybrid Interface, 2014.
[38] J.L. Smialek, Oxidation of Al2O3 scale-forming MAX Phases in turbine environments, Metall. Mater. Trans. A 49 (3) (2018) 782–792.
[39] M.A. Dayananda, Average effective interdiffusion coefficients in binary and multicomponent alloys, Defect and Diffusion Forum, Trans Tech Publ 1993, pp. 521–536.
[40] S. Brennan, K. Bermudez, N.S. Kulkarni, Y. Sohn, Interdiffusion in the Mg-Al system and intrinsic diffusion in β-Mg 2 Al 3, Metall. Mater. Trans. A 43 (11) (2012) 4043–4052.
[41] R.C. Reed, The Superalloys: Fundamentals and Applications, Cambridge University Press, 2008.
[42] E.C. Santos, K. Kida, P. Carroll, R. Vilar, Optimization of laser deposited Ni-based single crystal superalloys microstructure, Adv. Mater. Res. (2011) 1405–1414 Trans Tech Publ.
[43] R. Hobbs, M. Karunaratne, S. Tin, R. Reed, C. Rae, Uphill diffusion in ternary Ni–Re–Ru alloys at 1000 and 1100° C, Mater. Sci. Eng. A 460 (2007) 587–594.
[44] R. Krishna, Uphill diffusion in multicomponent mixtures, Chem. Soc. Rev. 44 (10) (2015) 2812–2836.
[45] M. Karunaratne, S.L. Ogden, S.D. Kenny, R.C. Thomson, A multicomponent diffusion model for prediction of microstructural evolution in coated Ni based superalloy systems, Mater. Sci. Technol. 25 (2) (2009) 287–299.
[46] S. Datta, R. Filipek, M. Danielewski, Interdiffusion issues in Pt-modified NiAl coatings, Defect and Diffusion Forum, Trans Tech Publ 2002, pp. 47–60.
[47] Z. Sun, S. Li, R. Ahuja, J.M. Schneider, Calculated elastic properties of M2AlC (M = Ti, V, Cr, Nb and Ta), Solid State Commun. 129 (9) (2004) 589–592.
[48] J.M. Behm, C.A. Arrington, M.D. Morse, Spectroscopic studies of jet-cooled AlNi, J. Chem. Phys. 99 (9) (1993) 6409–6415.
[49] Z. Lin, M. Zhuo, Y. Zhou, M. Li, J. Wang, Atomic Scale Characterization of Layered Ternary Cr 2 Al C Ceramic, AIP, 2006.